International Journal of Heat and Mass Transfer 198 (2022) 123393

Contents lists available at ScienceDirect

International Journal of Heat and Mass Transfer

journal homepage: www.elsevier.com/locate/hmt

Strong linearity and effect of laser heating location in transient photo/electrothermal characterization of micro/nanoscale wires

Amin Karamati[a,‡], Nicholas Hunter[a,‡], Huan Lin[b], Hamidreza Zobeiri[a], Shen Xu[c], Xinwei Wang[a,*]

[a] Department of Mechanical Engineering, 271 Applied Science Complex II, Iowa State University, Ames, IA 50011, United States
[b] School of Environmental and Municipal Engineering, Qingdao University of Technology, Qingdao, Shandong 266033, China
[c] School of Mechanical and Automotive Engineering, Shanghai University of Engineering Science, Shanghai 201620, China

ARTICLE INFO

Article history:
Received 21 May 2022
Revised 10 August 2022
Accepted 26 August 2022

Keywords:
Transient Electro-Thermal (TET)
Transient Photo-Electro-Thermal (TPET)
Thermal diffusivity
Micro/nanoscale
Graphene fiber
Characterization scanning

ABSTRACT

In this work, using Transient Electro-Thermal (TET) and Transient Photo-Electro-Thermal (TPET) methods, a rigorous approach is developed for data processing and thermal characterization of micro/nanoscale wires. Applying a step DC current (TET) or step continuous wave laser beam (TPET), a voltage rise (or drop) occurs through the sample, which represents the temperature evolution in the sample. After taking the natural log of this transient voltage change, the data series greatly resembles a line with respect to time with a coefficient of $-\pi^2\alpha/L^2$ (α: thermal diffusivity, L: sample length). So, instead of typical nonlinear raw data fitting, the linear fitting can be effectively exploited, which makes it possible to obtain the fitting uncertainty (or the uncertainty of thermal diffusivity). However, it is shown that there is a nonlinearity part at the beginning of the logarithmic voltage (temperature) that should be excluded from linear fitting. Furthermore, the effect of laser beam location on the sample in the TPET measurement is investigated. It is unraveled that except the locations close to the sample ends, the irradiated location on the sample makes negligible difference in the result for thermal diffusivity measurement. The thermal diffusivity of our microscale graphene fiber is measured to be $7.46 \times 10^{-7}\mathrm{m^2s^{-1}}$ and $6.93 \times 10^{-7}\mathrm{m^2s^{-1}}$ (averaged over different locations) with the TET and TPET techniques respectively. The uncertainty of fitting is determined to be in the order of $\sim 10^{-9}\mathrm{m^2s^{-1}}$, confirming excellent linearity and measurement accuracy.

1. Introduction

Thermophysical properties of micro/nanoscale materials are critical to the thermal design and manufacturing of the related devices and energy conversion [1–4]. Up to now, several techniques have been developed to measure the thermophysical properties of micro/nanoscale wires. The 3ω technique [5–8], optical heating and electrical thermal sensing (OHETS) technique [9,10], the micro-bridge method [11–14], pulse laser-assisted thermal relaxation (PLTR) technique [15–17], transient electrothermal (TET) and transient photon-electro-thermal (TPET) techniques [18–24] are the most popular ones that have been used by researchers. However, there are some limitations regarding their utilization. For instance, the 3ω method necessitates the sample to have a linear I–V behavior and cannot be used for many semi-conductive one-dimensional micro/nanoscale samples [18]. The OHETS method suffers from both a long-running time (same as the 3ω method) as well as low signals [18]. The TET and TPET techniques, on the other hand, can be used to measure a wide variety of metallic, nonconductive, and semi-conductive micro/nanostructures with a significantly greater signal level in a much shorter time (typically in less than a second) [18]. The micro-bridge method is facing some challenges such as accurate evaluation of the thermal contact resistance and difficult device fabrication and sample transfer [25]. On the other hand, the TET, TPET, and PLTR methods are easy to operate and produce highly accurate results for thermophysical properties. The PLTR technique has the capability of measuring short wires with relatively high thermal conductivity/diffusivity [15]. Wang et al. [26] evaluated the thermal diffusivity of a $\sim$ 5mm platinum wire via TPET, and it was calculated to be $2.45 \times 10^{-5}\mathrm{m^2s^{-1}}$, being fairly consistent with the reference value of $2.51 \times 10^{-5}\mathrm{m^2s^{-1}}$. In a recent study, Xu et al. [24] measured the thermal diffusivity of CNT bundle to be $5.25 \times 10^{-5}\mathrm{m^2s^{-1}}$with the TET technique, which was in good agreement with previous reports [26–28].

* Corresponding author.
E-mail address: xwang3@iastate.edu (X. Wang).
‡ Equal contribution authors.

https://doi.org/10.1016/j.ijheatmasstransfer.2022.123393
0017-9310/

Table 1
Literature review on the thermal characterization of GF.

Sample	Thermal Conductivity k ($W\ m^{-1}\ k^{-1}$)	Thermal diffusivity α ($m^2\ s^{-1}$)	Ref.
Graphene fiber	1.14-1.18	$\sim 2 \times 10^{-6}$	[39]
Graphene fiber	149.7	-	[40]
Highly Crystalline GF	1480	-	[41]
rGO fiber	1435	-	[42]
Graphene fiber	1290	-	[29]
Macroscopic GF	1575±81	-	[31]

Due to superb properties such as high electrical (up to 2.24×10^7 Sm^{-1}) and thermal conductivities, considerable flexibility along with excellent mechanical strength, graphene fibers (GFs) have been recognized as a type of appealing micro/nanofibers for researchers to work on [29–31]. They can have a wide range of applications from medical, wearable supercapacitors, and energy storage devices to human activity monitors [32–34]. Having a great capacity to be used in several emerging science fields [34], thermal characterization of GFs is of paramount importance. As shown in Table 1, to our best knowledge, only few studies have been published reporting the thermal properties of GFs, such as thermal conductivity and thermal diffusivity. Therefore, in addition to our paper's main goal, which is a new data processing method in the thermal characterization of micro/nanoscale wires, we tried to further investigate graphene fibers' thermal behavior as it has not been studied well. Therefore, the thermal diffusivity of GFs will be presented by the new approach of data processing in this paper.

In the TET and TPET techniques, the thermal diffusivity is obtained by nonlinear fitting of the experimental data. However, determination of the fitting uncertainty is still not available, partly due to the very complicated relationship between temperature rise (or fall) and time. In this study, a rigorous analysis is conducted for data fitting in order to obtain the thermal diffusivity and the corresponding uncertainty of microscale GF, which can be used for any other samples. In fact, this analysis takes advantage of linear regression to assess the uncertainty of the fitting. Next, it will be shown that utilizing the TPET method during which a laser is used to excite the sample, the location of the laser spot on the sample does not affect the thermal characterization of the sample using our new data processing method, particularly the value we obtain for the thermal diffusivity of the sample.

2. Strong linearity in the TET technique

2.1. Linearity relation: effect of starting point

Our lab introduced the TET technique in 2007 [18]. It has been demonstrated to be extremely effective in tracing the transient temperature change of fiber- or film-like materials and measuring their thermal diffusivity with great uncertainty (better than 5%) [19,20,23]. The inset in Fig. 1 shows a schematic illustration of the TET technique. In this method, a step DC current is used to induce an abrupt voltage rise by Joule heating. The thermal diffusivity is then calculated using the transient temperature change over the sample. The heat conduction in the sample can be assumed to be one-dimensional due to its high length-diameter ratio. Ultimately, the thermal diffusivity is calculated using the one-dimensional heat transfer model and the transient temperature response over the bundle [18],

$$T^* = \frac{96}{\pi^4} \sum_{m=1}^{\infty} \frac{1 - \exp\left[-(2m-1)^2 \pi^2 \alpha t / L^2\right]}{(2m-1)^4} \tag{1}$$

where T^* is a dimensionless temperature rise that is normalized by the steady-state temperature increase under the same Joule heating. $\alpha$and L are the thermal diffusivity and length of the sample respectively. This temperature rise has been averaged on the whole length of the sample. When the time is normalized to the Fourier number as $Fo = \alpha t / L^2$, for any material with any length, Eq. (1) shows that the normalized temperature rise follows the same form with regard to Fo [18]. Fig. 1a depicts the calculated T^* versus Fo based on the Eq. (1). For our theoretical study part, the length of the sample is 2 mm, and the thermal diffusivity is $9 \times 10^{-7} m^2 s^{-1}$. Based on this figure, it is shown that after $Fo = 0.3$, T^* reaches the value of 0.95. To the right axis of Fig. 1a, $\ln(1 - T^*)$ has been presented versus Fo. What one can clearly realize from this figure is that there is solid linearity in $\ln(1 - T^*)$ values vs. Fo for the theoretical study of the TET. This is crucial to the next steps we are going to take in this research. From the theoretical calculations of the problem, we can deduce that the physical model for the non-dimensional temperature would be in the form of $T^* = 1 - B\exp(-A\alpha t / L^2)$. So, we can readily conclude that $\ln(1 - T^*) = \ln(B) - A\alpha t / L^2$. Normalizing time to the Fourier number as $Fo = \alpha t / L^2$ we will have the equation in the form of:

$$\ln(1 - T^*) = \ln(B) - A \cdot Fo, \tag{2}$$

where "$-A$" will be the slope of the straight line. In this paper, we will use this equation to fit the data.

Although the $\ln(1 - T^*)$ well resembles a line, we will show that at the beginning, it takes a bit of time to become a completely straight line. The value of constant A (or slope) is calculated to check how much it takes from the beginning of the data series that deviation from the straight line diminishes. In other words, to the left axis of Fig. 1b we examine the variation of A with respect to Fo from which the fitting has been accomplished. It is clear that the value of A (or slope) varies with the starting point for the fitting until a certain point after which it reaches a constant value of π^2. Based on the left axis of Fig. 1b, without any data exclusion from the beginning (considering all data for the fitting), the A value is 9.885. Moreover, the fitting mean square error (MS_{Error}) with respect to Fo from which the fitting has been calculated is shown in Fig. 1b. MS_{Error} is defined as $\sum_{i=1}^{n} (Y_{fit} - Y_{act})^2 / n$, where n is the number of data points, Y_{fit} are the result of fitting for every point, and Y_{act} are the values of $\ln(1 - T^*)$ taken from the calculation of Eq. (1). Based on this graph, after $Fo = 0.009$ (or $T^* = 0.1$), the MS_{Error} value approaches its minimum value to a great extent. So, for the fitting with the exclusion of the data before $T^* = 0.1$, we will get a value of 9.877 for the coefficient A. Comparing $A =$ 9.877with π^2 results in less than 0.07%difference. Therefore, for the TET fittings in this paper, the data before $T^* = 0.1$ will not be included, and we will take A as π^2.

2.2. Experimental investigation and uncertainty

There are multiple strategies by which GFs can be prepared from graphene oxide. Using the chemical vapor deposition method (CVD) and Cu wires as the growing layer, Chen et al. [35] assembled quite long GFs (tens of centimeters). Other methods such as twisting-drawing [36] and low-temperature chemical reduction-induced self-assembly [37] have also been used to prepare GFs. In

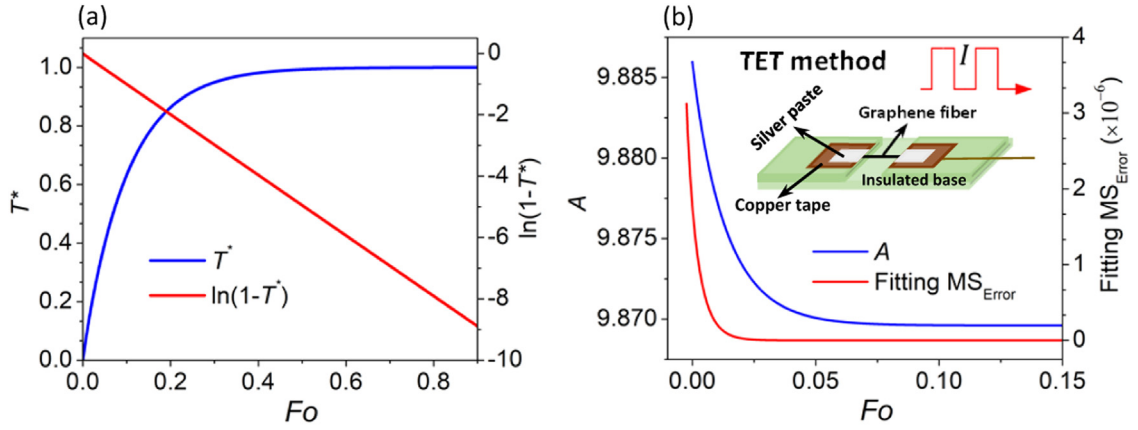

Fig. 1. (a) Left axis: non-dimensional temperature evolution due to the step dc current through the sample with *Fo* for the theoretical study of the TET technique. Right axis: $\ln\ln(1-T^*)$ vs. *Fo* for the theoretical study of the TET technique. (b) To the left axis: variation of coefficient *A* (slope of the fitted line) for the theoretical study of the TET vs. *Fo* from which the linear fitting has been performed. To the right axis: the corresponding fitting MS_{Error} vs. *Fo* for the theoretical study of TET. The inset is the schematic of the TET.

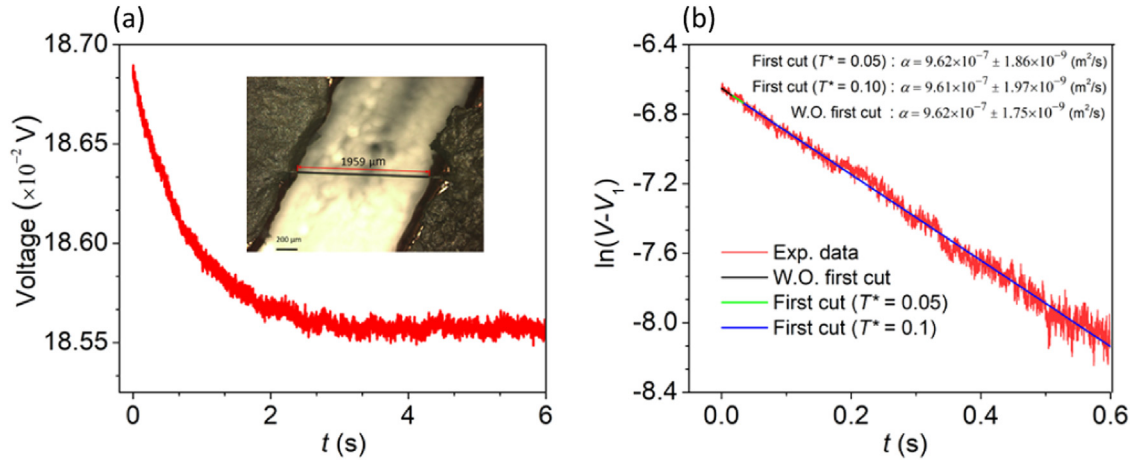

Fig. 2. (a) GF TET signal (experimental data) with time. The inset is the suspended GF of 1959 μm long. (b) Natural of GF TET voltage drop subtracted by the steady-state voltage (experimental data) with time. The three fittings are I) without initial cut, II) after $T^* = 0.05$, and III) after $T^* = 0.1$. The corresponding thermal diffusivities and uncertainties are also shown in the figure.

this work, we used a hydrothermal method to produce graphene fibers [38]. First, an appropriate amount of graphene oxide (GO) with the concentration of 30 mg/ml and DI water were mixed to have the aqueous suspension of GO. Then, the suspension was placed into an ultrasonic bath for one hour to achieve a homogenous suspension. Next, the suspension was injected into glass pipes with an inner diameter of 0.4 mm and a length of 10 cm. After sealing both ends of the pipes, the pipes were baked for two hours at 230°C. Ultimately, after extraction from the pipes, GFs of 20 ~ 30μm diameter were produced with good quality.

The inset in Fig. 2a depicts the suspended GF sample of 1959 μm length and 28.2 μm diameter. Also, as shown in the inset of Fig. 1b, the prepared GF has been placed on two electrodes attached to make it ready for the TET and TPET tests. Two electric wires are also used to connect to the ends of the sample to monitor the voltage variation during the experiment. Silver paste is then applied to the joints to make a good electrical and thermal connections between GF, electrodes and wires. To make the convection effect negligible, the experimental setup is placed in a vacuum chamber capable of reaching the vacuum level of less than 2 mTorr. The resistance of the sample was measured to be 3.71 kΩ, and a step DC current of 50 μA was fed to the sample. The value of the step current is chosen such that the transient phase of voltage change (temperature rise) is sensible, and the temperature rise is moderate to avoid sample structural damage.

In the theoretical study, we realized that there is a strong linear relation between $\ln(1-T^*)$ vs. *Fo* (or time). So, we can take advantage of this finding by establishing a link between normalized temperature and voltage as:

$$T^* = \frac{(V_0 - V)}{(V_0 - V_1)}, \tag{3}$$

where V_0 is the voltage at the beginning of the step current, and V_1 is the steady-state voltage. However, due to the minor fluctuations that exist even after the voltage has become steady, the voltages were averaged out for the steady state interval to determine the to-be-used V_1 value for the data analysis of the TET.

Taking the natural logarithm of Eq. (3), we can obtain:

$$\ln(V - V_1) = \ln(1 - T^*) + C, \tag{4}$$

where *C* is a constant. As it was shown earlier, $\ln(1-T^*) = \ln(B) - A\alpha t/L^2$, so we have:

$$\ln(V - V_1) = -A\alpha t/L^2 + D. \tag{5}$$

Hence having the voltage data from the experiment and the specified V_1, the fitting can be excellently performed. By the way, in Eq. (5), "$-A\alpha/L^2$" and D would be the slope and the intercept of the fitted line, respectively. This method will eliminate any raw data normalization while still retains the best data fitting accuracy.

Fig. 2b illustrates the results of $\ln(V-V_1)$ for the TET of the GF with respect to time. It should be mentioned that after passing the point of $T^*=0.8$, the fluctuations of $\ln(V-V_1)$ around the hypothetical line intensify greatly, therefore we exclude the data after $T^*=0.8$ from the fitting. Moreover, although there is strong linearity in this graph, as was discussed in the previous section (Fig. 1a), it was also recognized that there is a nonlinearity at the beginning of the $\ln(1-T^*)\sim Fo$ relation. So, to be able to use a constant $A=\pi^2$ in the fitting of experimental data, a part of data from the beginning should be excluded in the fitting process as well. Therefore, the linear fitting for three different cases of no cut, first cut from $T^*=0.05$, and first cut from $T^*=0.1$ was taken for data fitting and comparison. The corresponding values for the thermal diffusivity are 9.62×10^{-7}, 9.62×10^{-7}, and $9.61\times10^{-7}\mathrm{m^2s^{-1}}$ (Fig. 2b). As mentioned earlier, the convection heat transfer in the sample was considered negligible during the TET and TPET tests as it is put in a vacuum chamber. The radiation effect on the measured thermal diffusivity, however, can be evaluated using the expression of $16\varepsilon\sigma T^3L^2/\pi^2D\rho c_p$in which ε and σ are emissivity and the Stefan–Boltzmann constant [21]. For the GF, ε is considered to be 1 and T is the room temperature during the test, which is about 295 K. Taking the ρc_p of GF as graphite to be $\sim1.5\times10^6\mathrm{Jm^{-3}K^{-1}}$(this value has been recently investigated by our group and will be published soon), the calculated value for the radiation effect becomes $2.15\times10^{-7}\mathrm{m^2s^{-1}}$. Therefore, the latter value should be subtracted from the fitting results of α to obtain the real value for the thermal diffusivity of the GF. So, for the cases of no cut, first cut from $T^*=0.05$, and first cut from $T^*=0.1$, the real α values would be 7.47×10^{-7}, 7.47×10^{-7}, and $7.46\times10^{-7}\mathrm{m^2s^{-1}}$ respectively. It is noted that our measured thermal diffusivity is much lower than that ($\sim2\times10^{-6}\mathrm{m^2s^{-1}}$) reported in Ref. [39] for GF. Such difference could be caused by the sample's density, structure, and impurity levels. Eventually, the structure variation among samples might have been the main source of difference in the thermal diffusivity values.

The standard errors of the calculated α value for these three cases were $\pm1.75\times10^{-9}$, $\pm1.86\times10^{-9}$, and $\pm1.97\times10^{-9}$ $\mathrm{m^2s^{-1}}$, respectively. It is worth mentioning that these standard errors are in fact the uncertainties of fitting, and it does not include the uncertainty of other factors, such as length and voltage measurement, etc.

3. Strong linearity in TPET technique and effect of laser heating spot location

3.1. Linearity relation: effect of starting point and laser location

The TPET technique was also used in this study to investigate the thermal diffusivity of graphene fiber. The major difference between this method and TET is just the heating source of the tested sample, which is step laser irradiation rather than step current. The schematic of the TPET is illustrated as an inset in Fig. 3b. In this technique that was first introduced by our lab [26], the micro/nanoscale sample is suspended between two electrodes, and a step continuous wave (CW) laser irradiates the whole sample uniformly. As the temperature of the sample rises, its resistance changes and a transient change of voltage occurs through the sample, which is used to extract the thermal diffusivity of the sample. A low DC current is also passed through the sample to detect the voltage change during the experiment. Besides, due to the negative resistance temperature coefficient (RTC) of GF, after laser irradiation and heating up of the sample, the voltage through the sample drops.

As far as the physical model development of TET and TPET techniques is concerned, the temperature distribution in the 1-D wire/fiber can be described as [18]:

$$T(x,t)=T_0+\frac{\alpha}{k}\int_{\tau=0}^{t}\int_{x'=0}^{L}q_0G_{X11}dx'd\tau, \tag{6}$$

where T_0 is the temperature of the electrode (room temperature), k is the thermal conductivity of the sample, q_0 is the heating power per unit volume, and G_{X11} is the Green's function that is expressed as:

$$G_{X11}\left(x,t|x',\tau\right)=\frac{2}{L}\sum_{m=1}^{\infty}\exp\left[-m^2\pi^2\alpha(t-\tau)/L^2\right]\times\sin\left(m\pi\frac{x}{L}\right)\sin\left(m\pi\frac{x}{L}\right). \tag{7}$$

Integrating the Eq. (6) as $T(t)=\frac{1}{L}\int_{x=0}^{L}T(x,t)dx$ will result in Eq. (1), which is the solution for the TET. Eq. (6) can also be used for the TPET technique if the laser beam (heating power) covers the whole sample uniformly.

In this work, we will study the scenario that a localized laser heats up the sample at a certain location. Based on the schematic of TPET illustrated in the inset on Fig. 3b, we assume that a lined laser spot size of l width irradiates the sample on the location of x from the beginning of the sample. So, the dimensionless temperature for the TPET with local irradiation of laser spot will be obtained as

$$T^*=\frac{1}{Z}\sum_{m=1}^{\infty}\left\{\frac{\cos\left[(2m-1)\pi x/L\right]-\cos\left[(2m-1)\pi(x+l)/L\right]}{(2m-1)^4}\times\left[1-\exp(-(2m-1)^2\pi^2\alpha t/L^2)\right]\right\}, \tag{8}$$

where

$$Z=\sum_{m=1}^{\infty}\left\{\frac{\cos\left[(2m-1)\pi x/L\right]-\cos\left[(2m-1)\pi(x+l)/L\right]}{(2m-1)^4}\right\}. \tag{9}$$

Equation (8) is then solved for different locations where the line laser beam irradiates the sample and the corresponding results of $\ln(1-T^*)$vs. Fo are given in Fig. 3a. The length of the sample for the theoretical study of the TPET has been considered to be 2 mm, and the thermal diffusivity to be $9\times10^{-7}\mathrm{m^2s^{-1}}$. . As can be seen at the beginning of temperature changes, for different locations of the laser spot, it takes some certain time for them to become completely linear. The extent of this nonlinearity, however, is different for each different laser spot location. Also, shown in the inset of Fig. 3a, the level of nonlinearity is considerable when the laser spot location is near the edges of the sample and electrodes. It becomes weakened as the laser spot goes towards the middle of the sample. The other significant fact that we can observe is that after a certain time, all the curves become fully linear following the same slope.

As we discussed before, for the TET technique, we deduced the equation of the form $\ln(1-T^*)=\ln(B)-A\cdot Fo$ for the relation between T^* and Fo in which "$-A$" is the slope of the fitted line. Here we do the same for the TPET temperature evolution. Fig. 3b represents the A values with regard to Fo with excluding some nonlinear data from the beginning until Fo. It is evident that at the beginning, the variation of A value vs. Fo differs for different locations where laser irradiates the sample. The closer the laser spot to the ends of the sample, the more the deviation of the curves from linearity. Moreover, the initial deviation of the A coefficient from the constant value of π^2 is weaker for the laser locations of $\sim0.25L$ ($x=0.5$ mm) to $0.75L$ ($x=1.5$ mm) (L: sample's length),

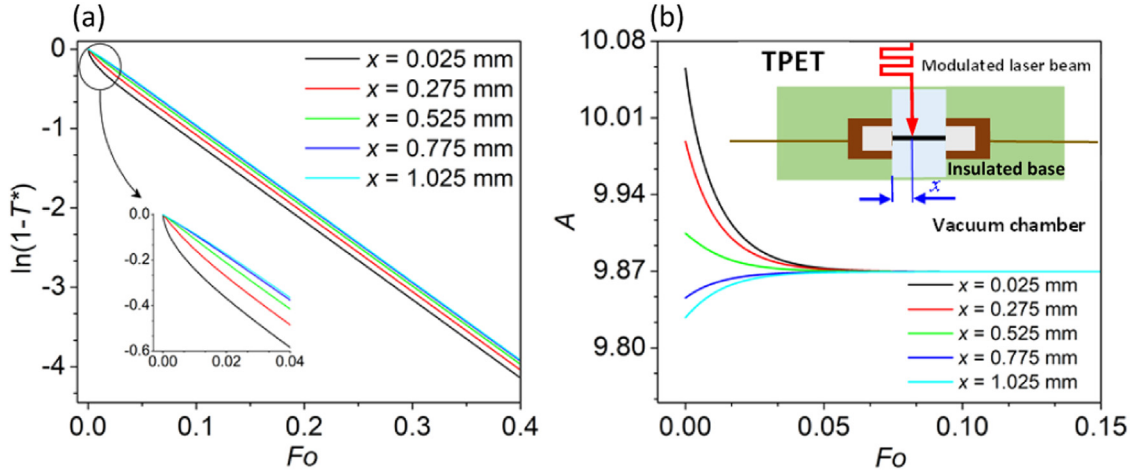

Fig. 3. (a) $\ln(1-T^*) \sim Fo$ relations under different laser location heating. The inset is the magnified illustration of the initial part of the graphs. (b) The variation of A coefficient (slope of fitting) for different laser locations with respect to Fo from which the fitting has been done (the theoretical study of TPET). The inset is the schematic of the TPET technique.

and the difference is less than 0.3% even considering the whole temperature evolution. It is also clear that all the curves finally reach the constant of 9.870 (almost π^2), which is exactly the same value we had observed for the TET technique. Moreover, all the curves reach the constant value of π^2 after Fo reaches 0.06, indicating that all the curves become completely linear afterward and they are parallel.

3.2. Effect of laser location: experiment

In this study, using a cylindrical lens, the laser spot was reshaped to a narrow line of 0.1 mm width. We investigated the effect of laser spot location on the thermal diffusivity value measured using the TPET technique. The sample was placed at the focal plane of the cylindrical lens to achieve the narrowest line of the laser beam. A 532 nm laser (DPSS Inc.) connected to a modulator was utilized as the heating source. The frequency of the laser beam was set to be 0.1 Hz with a square wave shape using the modulator. Shown in the inset of Fig. 3b, the setup was then placed in a vacuum chamber to run the experiment under < 2 mTorr environment to make the convection effect negligible. The last but not least, to calculate the optimum magnitude of the to be used DC current for the TPET method (I_1), the current magnitude applied for the TET technique (I_0) is used for analysis. As mentioned for the TET, the step current of I_0 is chosen such that the smallest sensible transient voltage drop (ΔV_0) is observed in the sample before reaching the steady state voltage (V_0). Assuming the resistance of R for the sample, the amount of induced Joule's heating (Q_0) and the V_0 will be RI_0^2 and RI_0respectively. Also, let us assume the temperature change in the sample is ΔT_0 due to the applied current. So, the ratio of the voltage drop over the steady state voltage can be calculated as $A_{\text{TET}} = \Delta V_0/(RI_0)$. For the TPET, on the other hand, in addition to the DC current, a laser beam irradiates the sample and induce a transient temperature change in the sample. Passing a DC current of I_1 through the sample, the corresponding induced temperature change (ΔT_1) can be calculated as$\Delta T_1 = (I_1/I_0)^2 \Delta T_0$. Upon laser irradiation, an additional temperature change occurs in the sample ($\Delta T'$). So, the ratio of the voltage drop (due to the laser irradiation) in terms of the TET voltage drop ratio can be written as$B_{\text{Laser}} = \Delta T'/\Delta T_0 \cdot A_{\text{TET}}$. Also, for the TPET, we want the voltage drop caused by the applied current and laser irradiation to be the smallest sensible one (i.e., ΔV_0). So, we can conclude that $RI_1.B_{\text{Laser}} = \Delta V_0$. Reorganizing the above expressions, we will have$\Delta T' = \Delta T_0 I_0/I_1$. Ultimately, the total temperature change can be expressed as:

$$\Delta T_{\text{Total}} = \left[\left(\frac{I_1}{I_0}\right)^2 + \frac{I_0}{I_1}\right]\Delta T_0 \tag{10}$$

To have the lowest temperature rise in the sample based on Eq. 10, the relation between the TPET and the TET DC current magnitudes will be $I_1 = 0.79 I_0$. This relation provides the good guidance for TPET current selection.

A DC current of 20 μA was used during the TPET in our experiment. To have approximately the same voltage drop (temperature rise) for different locations, the amount of laser power was adjusted during the experiment. The closer the laser beam to the ends of the sample, the more power was needed to have a clear signal of the transient voltage change. Moreover, the laser power value was controlled not to have a high temperature rise through the sample, so the sample's structure was not changed. Fig. 4a shows the ratio of the voltage drop under uniform laser power irradiation at different locations. It can be seen that as the laser spot location moved from the ends of the sample toward the middle, the ratio of voltage drop over laser power increases. For instance, for the laser location of $x = 0.025$ mm, the range of this ratio is from 7.25-7.20 mV/mW, while the range for the location of $x = 1.025$ mm is from 38.06 to 37.5 mV/mW. Having almost the same voltage drop value for different locations, this noticeable difference simply means that more laser power was needed for the locations near the ends of the sample. In other words, with the same amount of laser power, the signal or the voltage drop for the locations closer to the ends of the sample was weaker compared to the middle ones. This is because when the laser spot is close to the sample's ends, the sample's total thermal resistance is smaller. Therefore, a lower temperature rise was induced under the same laser heating. Ultimately, a power range of nearly 2-10 mW was used during the laser scanning over the sample. Fig. 4b depicts the results of $\ln(V - V_1)$ for different locations with time. It should be noted that for every location, to determine the to-be-used V_1, we examined a range of V_1 within the fluctuation range to check which V_1 gives the smallest fitting deviation.

It is clear that all the curves for different locations well resemble a line, and their slope is used to determine the thermal diffusivity of the sample for different laser spot locations. It should be noted that same as the TET, the data between $T^* = 0.1$ and $T^* = 0.8$ were used for fitting of the TPET, too. All the fittings show excellent agreement with the measured data.

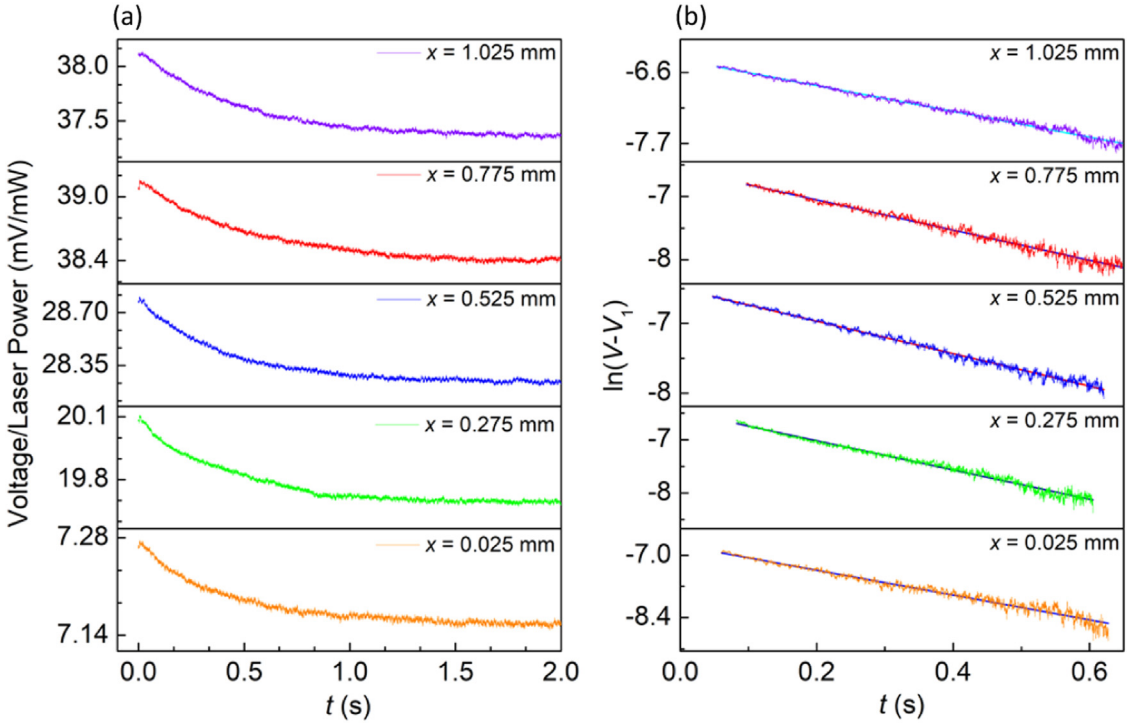

Fig. 4. (a) The voltage drop under unit laser power irradiation during the TPET experiment for different locations of the GF sample with time. (b) Natural of the GF TPET voltage drop subtracted by the steady-state voltage (experimental data) along with the linear fitting vs. time for different laser locations.

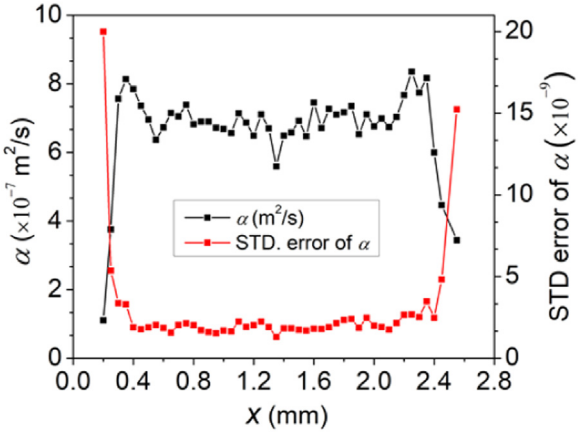

Fig. 5. Thermal diffusivity values for different laser heating locations obtained via the TPET technique. Also shown in the figure is standard error of the obtained thermal diffusivities.

The results of the determined thermal diffusivity of the GF sample with respect to the laser heating location are shown in Fig. 5. Based on this figure, except the locations near the sample two ends, it is evident that the α value remains almost constant with respect to the laser beam incident location. This finding is absolutely crucial because it leads to a vital discovery: for thermal characterization of a micro/nanoscale wire with the TPET technique, the laser beam incidence location on the sample is not critical. For the locations close to the sample's ends, due to the low thermal resistance between the laser irradiated location and the electrodes, more laser power was needed to have a good voltage signal. So, this higher laser power could have changed the boundary conditions (room temperature) that has been assumed for the heat transfer model for the TPET technique. Ultimately, the average value of α for different laser locations is $\sim 9.17 \times 10^{-7}\mathrm{m^2s^{-1}}$, which becomes $\sim 7.02 \times 10^{-7}\mathrm{m^2s^{-1}}$ after the radiation effect is subtracted, likewise what was done for the TET earlier. After excluding the locations near the ends of the sample, the average value of α becomes $\sim 9.08 \times 10^{-7}\mathrm{m^2s^{-1}}$, and $\sim 6.93 \times 10^{-7}\mathrm{m^2s^{-1}}$after subtraction of radiation effect. The difference between the latter and the value measured via the TET technique ($\sim 7.46 \times 10^{-7}\mathrm{m^2s^{-1}}$) is about 7.1%.

Another important fact is that the thermal diffusivity value obtained via the TPET method is somewhat lower than that of the TET technique ($\sim$ 7%). This difference could be caused by two factors. First, for most materials, as the temperature goes up, the overall thermal reffusivity increases [22]. So, the thermal diffusivity, as the inverse of the thermal reffusivity, will decrease as the temperature of the material goes up. The overall temperature rise of the sample under the TPET test is generally higher than that under the TET measurement as both the current and laser irradiation are applied to the sample, which can justify the difference we observe between the thermal diffusivity results of the TET and TPET methods. The temperature change of the sample during the TET is due to the step DC current and can be calculated from $\Delta T_0 = RI_0^2L/12kA_s$, where A_s is the cross sectional area the sample. The thermal conductivity of the GF can be calculated as $k = \alpha\rho c_p$and the ρc_p of graphite ($\sim 1.5 \times 10^6\mathrm{Jm^{-3}K^{-1}}$) can be used for the GF. For the TPET, on the other hand, the temperature change in the sample occurs because of the DC current as well as the step laser irradiation. The corresponding values of which can be calculated from $\Delta T_1 = (I_1/I_0)^2\Delta T_0$and $\Delta T' = \Delta T_0[(\Delta V_1/V_1)/(\Delta V_0/V_0)]$. Here $\Delta V_0$and ΔV_1 are the voltage drops due to the step DC current and step laser irradiation respectively. For the case of our GF sample, the temperature rise during the TET and the TPET are calculated to be $\sim$ 2.2 K and $\sim$ 7 K respectively.

Second, as discussed earlier, the methods we utilized for the TET and the TPET data fitting were slightly different in V_1 selection.

The reason for adopting two different fitting methods is that using the average V_1 method for the TPET data fitting was not satisfactory due to the fluctuations in the voltage data series. In Fig. 5, the values of the standard error (uncertainty) values for the calculated α at different laser locations are also presented. The uncertainty variation of α is compatible with the α variation vs. laser location as it is higher in the vicinity of the sample ends, and it bounces around $2.5 \times 10^{-9}\mathrm{m}^2\mathrm{s}^{-1}$. Based on the uncertainty curve in Fig. 5, it can be concluded that the trustable range to obtain the thermal diffusivity via the TPET method while the sample is irradiated locally is almost from 20% to 80% of its length. This is important that the typical level of uncertainty for the linear fitting in this study is smaller than the fitting value by more than two orders of magnitude, and the relative uncertainty is about 0.28%.

4. Conclusion

In this work, a new approach was developed for data processing and thermal characterization of micro/nanoscale wires or fibers using the TET and TPET techniques. In the TET method, it was uncovered that there is a significant linear relation between $\ln(1-T^*)$ and time, which can be employed for linear data fitting. It was shown that doing the linear fitting for the $\ln(1-T^*)$ with respect to Fo gives a value of $\sim\pi^2$ for the slope (coefficient A) after excluding the initial data before $T^*=0.1$. However, even considering all the data, the value we get for coefficient A only deviates from π^2 by 0.15%. The value of π^2 was then used for the experimental data fitting to obtain the thermal diffusivity of the sample. The thermal diffusivity of the GF using this method via TET was measured to be $9.61 \times 10^{-7}\mathrm{m}^2\mathrm{s}^{-1} \pm 1.97 \times 10^{-9}$ using the data between $T^*=0.1$ and $T^*=0.8$. The real α value for the TET method after radiation effect subtraction was $7.46 \times 10^{-7}\mathrm{m}^2\mathrm{s}^{-1}$. For the TPET technique, it was discovered $\ln(1-T^*)\sim t$ quickly becomes linear and the ultimate value for the coefficient A is the same constant π^2 regardless of the laser heating location. In this technique, the scale of initial nonlinearity between $\ln(1-T^*)$ and time depends on the laser location on the sample, and the level of nonlinearity is higher when the laser spot is at the sample's two ends. Discarding the data before $T^*=0.1$, for the laser location of $x=0.025$ mm for a 2 mm long sample, the deviation (initial nonlinearity) of the corresponding coefficient A from π^2 is nearly 1.38%. In comparison, it becomes about 1.88% considering all the data for fitting. For the laser locations of 25% ($x=0.5$ mm) to 75% ($x=1.5$mm) on the sample, however, the deviation is much weaker (<0.3%). The experimental results well confirmed this finding. The difference in the thermal diffusivity value measured via the TET and the TPET (averaged over different laser locations on the sample) methods was ~ 7.1%, mainly due to the higher temperature rise in TPET measurement as well as various steady state voltages adopted for the fitting. (Eq. 2,4,7,9)

Credit author statement

X. Wang conceived the research idea. A. Karamati, Ni. Hunter, and X. Wang conducted program development, data analysis, experimental study, and data processing. H. Lin, H. Zobeiri, and S. Xu participated in experimental design, conduction, and data processing. All authors conducted physical model development and data physical interpretation. All authors participated in manuscript preparation.

Declaration of Competing Interest

The authors declare that they have no known competing financial interests or personal relationships that could have appeared to influence the work reported in this paper.

Data availability

Data will be made available on request.

Acknowledgment

Partial support of this work by US National Science Foundation (CBET1930866 and CMMI2032464 for X.W.), National Key Research and Development Program (2019YFE0119900 for H.L.), and Natural Science Foundation of Shandong Province (ZR2020ME183 for H.L) is gratefully acknowledged.

References

[1] Y. Fu, G. Cui, K. Jeppson, Thermal Characterization of Low-Dimensional Materials by Resistance Thermometers, Materials 12 (11) (2019) 1740 [Online]Available: https://www.mdpi.com/1996-1944/12/11/1740.
[2] J. Liu, P. Li, H. Zheng, Review on Techniques for Thermal Characterization of Graphene and Related 2D Materials, Nanomaterials 11 (11) (2021) 2787 [Online]Available: https://www.mdpi.com/2079-4991/11/11/2787.
[3] R. Wang, S. Xu, Y. Yue, X. Wang, Thermal behavior of materials in laser-assisted extreme manufacturing: Raman-based novel characterization, Int. J. Extrem. Manuf. 2 (3) (2020) 032004.
[4] Y. Zhao, et al., The fabrication, characterization and functionalization in molecular electronics, Int. J. Extrem. Manuf. 4 (2) (2022) 022003.
[5] D.G. Cahill, Thermal conductivity measurement from 30 to 750 K: the 3ω method, Rev. Sci. Instrum. 61 (2) (1990) 802–808.
[6] L. Lu, W. Yi, D. Zhang, 3ω method for specific heat and thermal conductivity measurements, Rev. Sci. Instrum. 72 (7) (2001) 2996–3003.
[7] L. Dong, et al., Thermal conductivity, electrical resistivity, and microstructure of Cu/W multilayered nanofilms, ACS Appl. Mater. Interfaces 12 (7) (2020) 8886–8896.
[8] T.-Y. Choi, D. Poulikakos, J. Tharian, U. Sennhauser, Measurement of the thermal conductivity of individual carbon nanotubes by the four-point three-ω method, Nano Lett. 6 (8) (2006) 1589–1593.
[9] Y. Xie, Y. Yue, X. Wang, Characterization of thermal conductivity, diffusivity, specific heat, Therm. Behav. Appl. Carbon-Base. Nanomater. Theor. Method. Appl. (2020) 57.
[10] L. Qiu, Y. Ouyang, F. Li, Experimental techniques overview, in: Micro and Nano Thermal Transport, Elsevier, 2022, pp. 19–45.
[11] L. Shi, et al., Measuring thermal and thermoelectric properties of one-dimensional nanostructures using a microfabricated device, J. Heat Transf. 125 (5) (2003) 881–888.
[12] K. Hippalgaonkar, J.H. Seol, D. Xu, D. Li, Experimental studies of thermal transport in nanostructures, in: Thermal Transport in Carbon-Based Nanomaterials, Elsevier, 2017, pp. 319–357.
[13] Y. Wang, N. Xu, D. Li, J. Zhu, Thermal properties of two dimensional layered materials, Adv. Funct. Mater. 27 (19) (2017) 1604134.
[14] X. Wang, et al., Measuring nanowire thermal conductivity at high temperatures, Meas. Sci. Technol. 29 (2) (2018) 025001.
[15] J. Guo, X. Wang, D.B. Geohegan, G. Eres, C. Vincent, Development of pulsed laser-assisted thermal relaxation technique for thermal characterization of microscale wires, J. Appl. Phys. 103 (11) (2008) 113505.
[16] J. Guo, X. Wang, D.B. Geohegan, G. Eres, Thermal characterization of multi-wall carbon nanotube bundles based on pulsed laser-assisted thermal relaxation, Funct. Mater. Lett. 1 (01) (2008) 71–76.
[17] J. Liu, M. Han, R. Wang, S. Xu, X. Wang, Photothermal phenomenon: Extended ideas for thermophysical properties characterization, J. Appl. Phys. 131 (6) (2022) 065107.
[18] J. Guo, X. Wang, T. Wang, Thermal characterization of microscale conductive and nonconductive wires using transient electrothermal technique, J. Appl. Phys. 101 (6) (2007) 063537.
[19] B. Zhu, et al., Novel Polyethylene Fibers of Very High Thermal Conductivity Enabled by Amorphous Restructuring, ACS Omega 2 (7) (2017) 3931–3944 2017/07/31, doi:10.1021/acsomega.7b00563.
[20] J. Liu, T. Wang, S. Xu, P. Yuan, X. Xu, X. Wang, Thermal conductivity of giant mono-to few-layered CVD graphene supported on an organic substrate, Nanoscale 8 (19) (2016) 10298–10309.
[21] J. Liu, Z. Xu, Z. Cheng, S. Xu, X. Wang, Thermal conductivity of ultrahigh molecular weight polyethylene crystal: defect effect uncovered by 0 K limit phonon diffusion, ACS Appl. Mater. Interfaces 7 (49) (2015) 27279–27288.
[22] Y. Xie, B. Zhu, J. Liu, Z. Xu, X. Wang, Thermal reffusivity: uncovering phonon behavior, structural defects, and domain size, Frontiers in Energy 12 (1) (2018) 143–157.
[23] H. Lin, S. Xu, X. Wang, N. Mei, Thermal and Electrical Conduction in Ultrathin Metallic Films: 7 nm down to Sub-Nanometer Thickness, Small 9 (15) (2013) 2585–2594.
[24] S. Xu, H. Zobeiri, N. Hunter, H. Zhang, G. Eres, X. Wang, Photocurrent in carbon nanotube bundle: graded seebeck coefficient phenomenon, Nano Energy 86 (2021) 106054.
[25] A. El Sachat, F. Alzina, C.M. Sotomayor Torres, E. Chavez-Angel, Heat transport control and thermal characterization of low-dimensional materials: A review, Nanomaterials 11 (1) (2021) 175.

[26] T. Wang, X. Wang, J. Guo, Z. Luo, K. Cen, Characterization of thermal diffusivity of micro/nanoscale wires by transient photo-electro-thermal technique, Appl. Phys. A 87 (4) (2007) 599–605.
[27] X. Huang, J. Wang, G. Eres, X. Wang, Thermophysical properties of multi-wall carbon nanotube bundles at elevated temperatures up to 830 K, Carbon 49 (5) (2011) 1680–1691.
[28] Y. Xie, et al., 19-Fold thermal conductivity increase of carbon nanotube bundles toward high-end thermal design applications, Carbon 139 (2018) 445–458.
[29] G. Xin, et al., Highly thermally conductive and mechanically strong graphene fibers, Science 349 (6252) (2015) 1083–1087.
[30] Y. Liu, Z. Xu, J. Zhan, P. Li, C. Gao, Superb electrically conductive graphene fibers via doping strategy, Adv. Mater. 28 (36) (2016) 7941–7947.
[31] G. Xin, et al., Microfluidics-enabled orientation and microstructure control of macroscopic graphene fibres, Nat. Nanotechnol. 14 (2) (2019) 168–175.
[32] M.C. McNamara, et al., Behavior of Neural Cells Post Manufacturing and After Prolonged Encapsulation within Conductive Graphene-Laden Alginate Microfibers, Adv. Biol. 5 (11) (2021) 2101026.
[33] H. Cheng, Q. Li, L. Zhu, S. Chen, Graphene Fiber-Based Wearable Supercapacitors: Recent Advances in Design, Construction, and Application, Small Methods 5 (9) (2021) 2100502.
[34] X. Zheng, Q. Hu, X. Zhou, W. Nie, C. Li, N. Yuan, Graphene-based fibers for the energy devices application: A comprehensive review, Materials & Design 201 (2021) 109476.
[35] T. Chen, L. Dai, Macroscopic Graphene Fibers Directly Assembled from CVD–Grown Fiber-Shaped Hollow Graphene Tubes, Angew. Chem. 127 (49) (2015) 15160–15163.
[36] B. Fang, et al., Handedness-controlled and solvent-driven actuators with twisted fibers, Materials Horizons 6 (6) (2019) 1207–1214.
[37] J. Li, J. Li, L. Li, M. Yu, H. Ma, B. Zhang, Flexible graphene fibers prepared by chemical reduction-induced self-assembly, J. Mater. Chem. A 2 (18) (2014) 6359–6362.
[38] Z. Dong, et al., Facile fabrication of light, flexible and multifunctional graphene fibers, Adv. Mater. 24 (14) (2012) 1856–1861.
[39] H. Lin, H. Dong, S. Xu, X. Wang, J. Zhang, Y. Wang, Thermal transport in graphene fiber fabricated by wet-spinning method, Mater. Lett. 183 (2016) 147–150.
[40] W. Ma, et al., Systematic characterization of transport and thermoelectric properties of a macroscopic graphene fiber, Nano Res. 9 (11) (2016) 3536–3546.
[41] P. Li, et al., Highly crystalline graphene fibers with superior strength and conductivities by plasticization spinning, Adv. Funct. Mater. 30 (52) (2020) 2006584.
[42] R. Jalili, et al., Scalable one-step wet-spinning of graphene fibers and yarns from liquid crystalline dispersions of graphene oxide: towards multifunctional textiles, Adv. Funct. Mater. 23 (43) (2013) 5345–5354.